IJCRT.ORG ISSN : 2320-2882

INTERNATIONAL JOURNAL OF CREATIVE RESEARCH THOUGHTS (IJCRT)

An International Open Access, Peer-reviewed, Refereed Journal

Dynamics And Control Of A Piezoelectric Hydraulic Motor For The Double-Acting Cylinder

[1]V K Sri Murali [1]st Author, [2]Gokul Kumar K [2]nd Author
[1]Research scholar[1]st Author, [2]Director and Professor [2]nd Author
[1]School of Mechanical Engineering (SMEC) [1]st Author,
[1]Vellore Institute of Technology, [1]st Author, Vellore, Tamil Nadu, India

Abstract: We have designed and simulated an advanced piezoelectric hydraulic diaphragm motor using MATLAB, validated it with experimental and numerical data from various research sources, and also through a three-dimensional model in ANSYS software. This piezoelectric hydraulic motor uses a seven-chamber piezoelectric setup comprising seven diaphragms. We analyzed the motor's performance under different external loads using Multiple Linear Regression (MLR), focusing on the sensing voltage from the middle three diaphragms (A3, A4, and A5). The electrodes are divided into a larger driving unit and a smaller sensing unit, employing diverse parametric and external loading methods. Our findings, listed in Tables 2, 3, and 4, reveal that the motor operates with a fixed sinusoidal voltage of 100V to 1000V and a frequency range of 60 Hz to 600 Hz. The optimal frequencies for external loads of 0.8, 3.0, and 10 Kg/mm² are 0.01378 rad/s, 0.004562 rad/s, and 0.003384 rad/s, with corresponding flow rates for A3, A5, and A7 being 0.554 mm³/s, 0.175 mm³/s, and 0.1715 mm³/s, respectively. This research highlights the significant capabilities and characteristics of the piezoelectric hydraulic diaphragm stack.

Keywords: Piezoelectric Hydraulic Motor, Dynamics, Materials and Nonlinear

1. Introduction

The recent development of an effective piezoelectric hydraulic diaphragm stack motor addresses the limitations of traditional piezoelectric linear motor systems. These limitations often arise from complex system layouts and the long-term contact friction and wear associated with them [1],[2], [3], [4]. To address contact friction, researchers have explored piezoelectric hydraulic linear motors, which use a liquid medium (liquid friction) to transfer power [4]-[5]. In recent years, the advancement of piezoelectric linear motors has established them as a significant branch of piezoelectric actuators. In 1993, Konishi et al. [4] First proposed a piezoelectric linear motor driven by piezoelectric stacking, achieving a maximum output power of 34 W and a maximum pump frequency of 300 Hz. By 2000, Mauck et al [6] developed a system that included a high-voltage piezoelectric stack, an accumulator, a check valve, a directional control valve, and a piston hydraulic actuator. This linear motor produced a blocked force of 271 N and an output velocity of 72.5 mm/s at 800 V and 60 Hz. In 2008, Kan et al. [7] introduced a piezoelectric linear motor composed of a piezoelectric membrane pump and a hydraulic cylinder, achieving a velocity of 14.5 mm/s and a thrust of 17.8 N at 140 V and 70 Hz. The following year, Xuan et al.[8] developed an integrated hybrid actuator driven by piezo stacks, which produced a maximum blocking force of 346 N and a no-load velocity of 101 mm/s at 250 Hz. In 2011, Kan et al.[9] created a piezoelectric linear motor powered by a multi-chamber piezoelectric micropump at 180 V and 280 Hz, achieving a thrust of 75 N and a velocity of 9.8 mm/s. By 2017, Li et al. developed a double-piezoelectric pump and hydraulic cylinder hybrid actuator are tested with different connections and drive modes for the piezoelectric pump, achieving a maximum velocity of 68.3 mm/s at 300 Hz. To improve the control accuracy of piezoelectric linear motors, external sensors have been incorporated into the systems. By 2009, Liaw et al.[10] developed a neural network-based dedicated position sensor for tracking the position of piezoelectric drive systems, eliminating positioning uncertainties between the end effector and the actuator. By 2016, Zhao et al.[11] proposed a hybrid pneumatic-driven piezoelectric flexible manipulator system capable of simultaneous position and vibration control. Their results demonstrated that the Self-Organising

Map (SOM) multiple-model inverse control algorithm could enhance control performance. While external sensors can improve the accuracy of piezoelectric linear motors, they also increase cost and complexity. Therefore, integrated sensors that enhance control performance without altering the mechanical structure have gained significant interest [12], [13], [14], [15], [16]. To monitor the flow rate of the piezoelectric pump—an essential component of the piezoelectric linear motor—Zhang et al.[17], [18], [19] presented an ultrathin curved-up microcantilever flow sensor made from insulator wafers. This sensor offers high sensitivity (1.5–3.5 μm/cm/s) for measuring a small flow (0–23 cm/s). In 2011, Fuchs et al.[20], [21], [22] introduced a piezoelectric peristaltic pump with an integrated sensor, enabling flow-rate sensing by fixing the sensor directly onto the membrane. By 2013, Zhang et al. [14] showcased a piezoelectric pump with an integrated sensor utilizing space-division multiplexing. These developments indicate that integrated sensors can significantly enhance pump performance [2], [8].

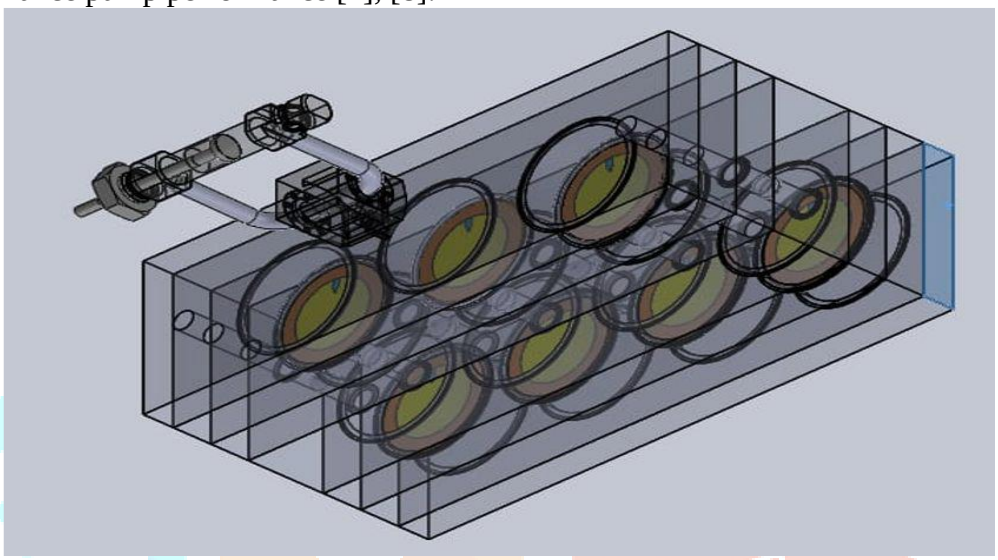

Fig 1: Three-Dimensional Piezoelectric Hydraulic Motor with Seven Hydraulic Chambers and Diaphragms.

2. Structure and working principle

The three-dimensional model of the piezoelectric hydraulic motor presented in this paper is illustrated in Fig. 1. This motor primarily consists of a serial connection between a seven-chamber piezoelectric motor and a hydraulic cylinder. The seven-chamber piezoelectric motor is made up of seven piezoelectric diaphragms (labelled A1, A2, A3, A4, A5, A6, and A7), seven chambers, and eight check valves. Each chamber unit comprises one piezoelectric diaphragm and one chamber, with each of the seven chamber units equipped with a check valve. The piezoelectric diaphragms are sequentially designated as A1, A2, A3, A4, A5, A6, and A7 in the direction of fluid movement. Diaphragms A1, A3, A5, and A7 are positioned at the inlet, middle, and outlet of the piezoelectric pump. The operation of the piezoelectric hydraulic motor is driven by AC signals, with a phase difference of 180° in the driving voltage applied to two adjacent piezoelectric diaphragms.

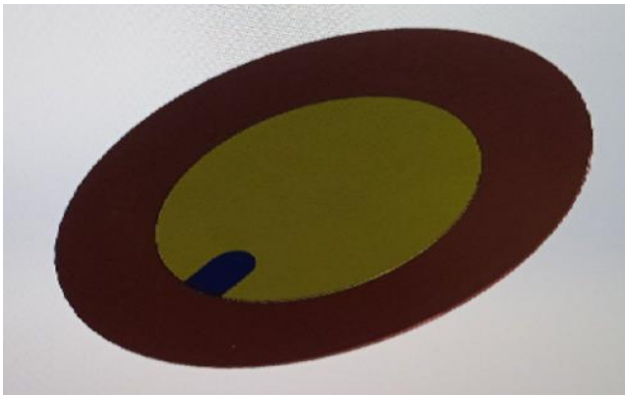

Fig 2. Structure of the piezoelectric transducer [2], [8]

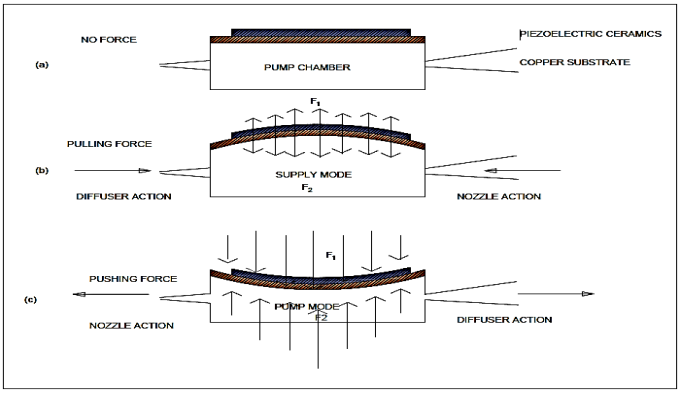

Fig 3. Working principle of the check valve motor and the force diagram of the piezoelectric transducer. (a) No force. (b) Pushing force & supply mode. (c) Pulling force & pump mode [2], [8]

When powered on, seven piezoelectric diaphragms will deform simultaneously. The first working state is illustrated in Fig. 3. Diaphragms A1, A3, A5, and A7 are subjected to a voltage that is opposite to the polarization direction of the PZT disc, while A2, A4, and A6 are connected to the same voltage as that of the PZT disc. As a result, A1, A3, A5, and A7 bend upward, while A2, A4, and A6 bend downward. Under pressure, and with the opening and closing of check valves, the liquid in the hydraulic cylinder enters the chamber unit of A1. Simultaneously, the liquid in the chamber units of A2 and A3 flows into the chamber units of A6 and A7, respectively. This configuration represents the second working state, as shown in Fig. 3. To operate the piezoelectric diaphragm, a voltage is applied in the opposite direction from the previous working condition. This causes diaphragms A1, A3, A5, and A7 to bend downward, while A2, A4, and A6 bend upward. Under pressure, the liquid in the chamber units of A1 and A3 flows into the chamber units of A4 and A6 through a check valve. Additionally, the fluid in the chamber unit of A7 enters the hydraulic cylinder via another check valve. When the pressure of the liquid in the hydraulic cylinder exceeds the resistance of the piston, the linear motor moves to the right by a distance D2 - D1 (where D2 - D1 represents the displacement of the piston rod). As an alternating voltage is continuously applied to the piezoelectric diaphragms, the system switches between the first and second working states repeatedly. This results in the hydraulic cylinder moving step by step, facilitating the stepping action of the piezoelectric hydraulic motor. The piezoelectric diaphragm consists of a metal substrate bonded to a PZT disc, as illustrated in Fig. 2. The surface of the PZT disc has a silver electrode layer. Each surface electrode of the seven piezoelectric diaphragms is divided into a larger driving unit and a smaller sensing unit using a segmented electrode method. The driving unit is activated by a sinusoidal voltage signal, while the sensing unit vibrates in conjunction with the metal substrate. Due to the direct piezoelectric effect, the sensing unit generates voltage signals that correspond to the vibration deformation. The sensing voltage (sinusoidal) from the sensing unit indicates changes in chamber volume, which relate directly to the output flow rate of the piezoelectric motor. Consequently, the velocity of the piezoelectric motor can be monitored using the sensing voltage (sinusoidal). Moreover, the multi-chamber pump's structure is more complex than that of a single-chamber pump, leading to interactions between the five piezoelectric diaphragms. In this study, we monitor the sensing voltages (sinusoidal) from diaphragms A3, A4, and A5 to determine the optimal sensing voltage signal, allowing for accurate velocity output display.

.

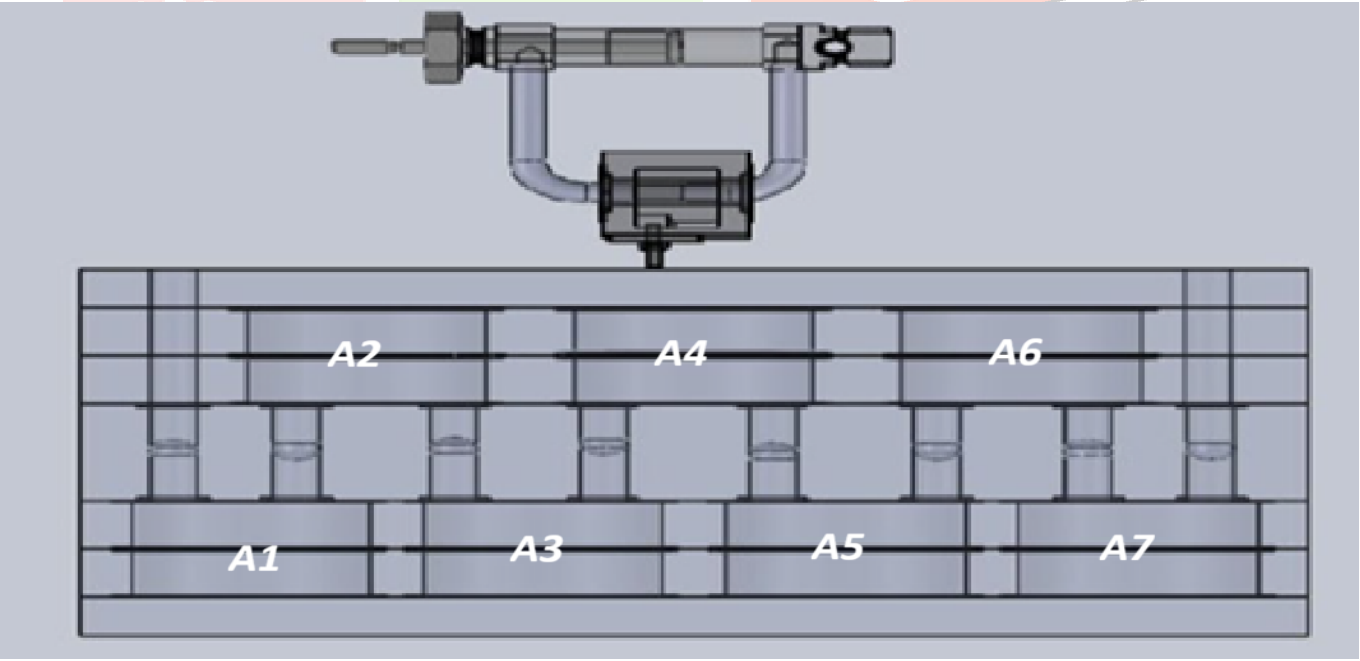

Fig 4: Piezoelectric Hydraulic motor with seven Chambers and seven diaphragms and eight Check valves.

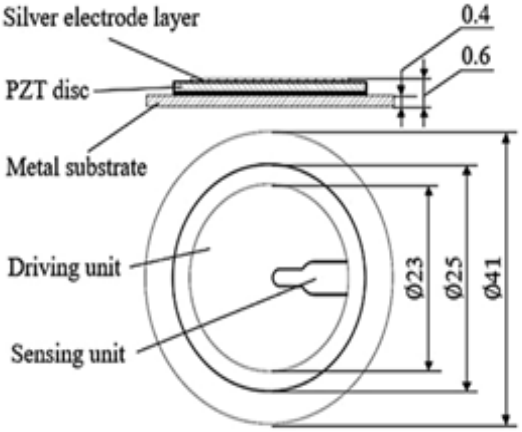

Fig 5: Piezoelectric Hydraulic Diaphragm

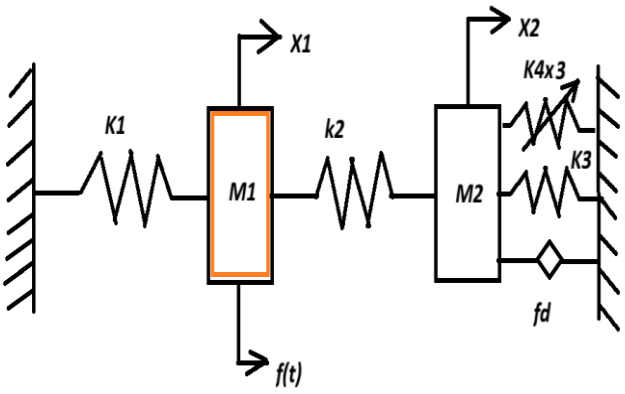

Fig 6: Free-body Diagram

3. Theoretical analysis

A serial-connection seven-chamber piezoelectric motor and a hydraulic cylinder. The piezoelectric motor pressurizes the liquid medium to realize the motion of the hydraulic cylinder. The dynamic model of the piezoelectric hydraulic motor vibration system, composed of a piezoelectric pump, fluid medium and hydraulic cylinder, is established as shown in Fig. 6. The motion differential equation of the system is

$$M_1 \ddot{x}_1 + k_1 x_1 - k_2 (x_1 - x_2) = f(t) \qquad (1)$$

$$M_2 \ddot{x}_2 + k_2 (x_2 - x_1) - k_3 x_2 - k_4 x_2^3 - fd\,\dot{x}_2 = 0 \qquad (2)$$

Where in M1 is the equivalent mass of piezoelectric diaphragms; M2 is the equivalent mass of the hydraulic cylinder and liquid; c is the equivalent damping coefficient of the hydraulic cylinder and liquid channel, oscillation velocity fractional damping and Displacement fractional damping; k1, k2, k3 are equivalent stiffness and k4 is a variable stiffness of piezoelectric diaphragms, fluid and hydraulic cylinder, respectively; x1 is the amplitude of the equivalent vibration of piezoelectric diaphragms; x2 is the equivalent driving displacement of the hydraulic cylinder; *f*(t) is the amplitude of the driving force of the piezoelectric diaphragms. For the convenience of analysis, piezoelectric diaphragms are regarded as springs with a different stiffness coefficient [8]. The mass of M1 is ignored, and the simplified Eq. (1) can be obtained as follows:

$$x_1 = \frac{f(t) - k_2 x_2}{(k_1 - k_2)} \qquad (3)$$

The Piezoelectric hydraulic motor system's mathematical model can be expressed as:

$$\ddot{x}_2 + \left[\frac{x_2 k_2 (k_1 - k_3 - k_2)}{M_2 (k_1 - k_2)}\right] - \left[\frac{k2\, f(t)}{M_2 (k_1 - k_2)}\right] - \left[\frac{k_4 x_2^3}{M_2}\right] - \left[\frac{fd * \dot{x}2}{M_2}\right] = 0 \qquad (4)$$

The Oscillation Viscosity Fractional Damping is

$$fd = \left[Ae\left(i\sqrt{\left(\frac{k}{m}\right) - \left(\frac{c}{2m}\right)^2} * t \right) + Be\left(-i\sqrt{\left(\frac{k}{m}\right) - \left(\frac{c}{2m}\right)^2} * t \right) * e\left(-\left(\frac{c}{2m}\right) * t \right) \right] \qquad (5)$$

The Displacement Fractional Damping is

$$\begin{cases} 0 & if\ \alpha = 2 \vee \alpha = 3 \\ \dfrac{2 * t^{2-\alpha}}{\Gamma(1-\alpha)(\alpha-1)(\alpha-2)} & if\ \alpha < 1 \vee (1-\alpha \wedge \neq 2 \wedge \alpha \neq 3 \wedge t \neq 0) \end{cases} \qquad (6)$$

Fractional Integral with different alpha(α) of 0.5, 1.0, 1.5 Vs Time

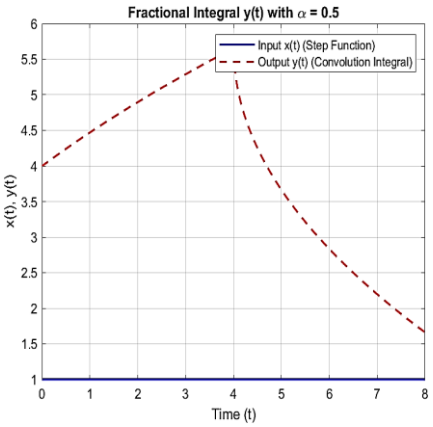

Fig 7: Fractional Integral for α=0.5

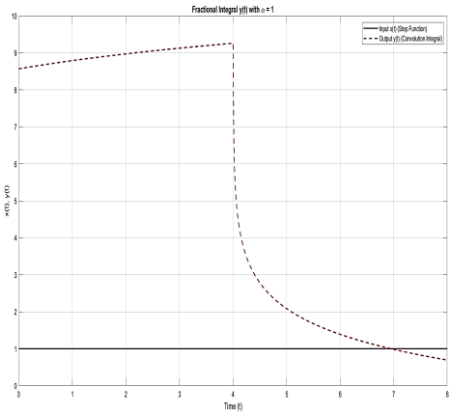

Fig 8: Fractional Integral for α=1.0

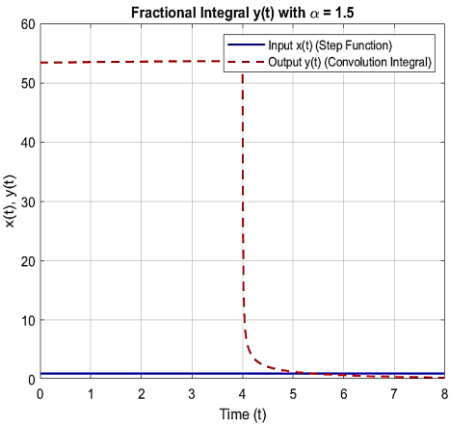

Fig 9: Fractional Integral for α=1.5

3.1. Newton's - Raphson method for the iterative loop

The Newton-Raphson method is used to converge on the solution. Further iterations quickly converge to a value with high precision.

$$t_{n+1} = t_n - \frac{f(t_n)}{f'(t_n)} = t_n - \frac{e^{t_n} + t_n - 5}{e^{t_n} + 1} \qquad (7)$$

3.2. Piezoelectric Matrix

Where [d] is the matrix for the direct piezoelectric effect and [d^t] is the matrix for the converse piezoelectric effect. The superscript E denotes a zero or constant electric field; the superscript T denotes a zero or constant stress field; and the superscript t denotes the transposition of the matrix.

3.2.1. Piezoelectric Effect

a) The piezoelectric effect results from the linear electromechanical interaction between the mechanical and electrical states in crystalline materials.
b) The piezoelectric effect is a reversible process.

3.2.2. Equations of piezoelectricity

Linear piezoelectricity is the combined effect of electrical and elastic mechanical behaviour. The following two laws define those behaviours.

a) The linear electrical behaviour of the material

$$D = \varepsilon E \Rightarrow D_i = \varepsilon_{ij} E_j \qquad (8)$$

D- is the electric charge density displacement (electric displacement)

ε- is the permittivity (free-body dielectric constant)

E- is electric field strength

b) Hooke's law for elastic materials

$$S=sT \Rightarrow Si_j=s_{ijkl}T_{kl} \qquad (9)$$

S- is Strain

s- is in compliance under short-circuit conditions

T- is Stress

These relations may be combined into so-called coupled equations, of which the strain-charge form is

$$S = sT + d^T E \qquad (10)$$
$$D = dT + \varepsilon E$$

Based on those equations, it has to be assigned in terms of their matrix equivalent.

$$\begin{bmatrix} S_1 \\ S_2 \\ S_3 \\ S_4 \\ S_5 \\ S_6 \end{bmatrix} = \begin{bmatrix} s_{11}^E & s_{12}^E & s_{13}^E & 0 & 0 & 0 \\ s_{21}^E & s_{22}^E & s_{23}^E & 0 & 0 & 0 \\ s_{31}^E & s_{32}^E & s_{33}^E & 0 & 0 & 0 \\ 0 & 0 & 0 & s_{44}^E & 0 & 0 \\ 0 & 0 & 0 & 0 & s_{55}^E & 0 \\ 0 & 0 & 0 & 0 & 0 & s_{66}^E = 2(s_{11}^E - s_{12}^E) \end{bmatrix} \begin{bmatrix} T_1 \\ T_2 \\ T_3 \\ T_4 \\ T_5 \\ T_6 \end{bmatrix} + \begin{bmatrix} 0 & 0 & d_{31} \\ 0 & 0 & d_{32} \\ 0 & 0 & d_{33} \\ 0 & d_{24} & 0 \\ d_{15} & 0 & 0 \\ 0 & 0 & 0 \end{bmatrix} \begin{bmatrix} E_1 \\ E_2 \\ E_3 \\ E_4 \\ E_5 \\ E_6 \end{bmatrix} \qquad (11)$$

According to Eq. (3), the natural frequency ω_n is related to the equivalent mass M2, along with the equivalent stiffness k1/ k2/ k3 and the varying stiffness of k4. When the parameters and constants of the piezoelectric hydraulic motor are considered, the natural frequency ω_n increases with the equivalent stiffness of the hydraulic cylinder k3 and k4. The equivalent stiffness of the hydraulic cylinder k3/k4 is positively correlated with the external load and varying stiffness k4. Therefore, the natural frequency ω_n will increase with the external load. For a multi-chamber piezoelectric motor, the monitoring performance of piezoelectric diaphragms at different positions will be different. The piezoelectric diaphragms near the inlet and outlet are highly affected by the fluid impact and cannot accurately reflect the change in flow rate.

$$\begin{bmatrix} D_1 \\ D_2 \\ D_3 \end{bmatrix} = \begin{bmatrix} 0 & 0 & 0 & 0 & d_{15} & 0 \\ 0 & 0 & 0 & d_{24} & 0 & 0 \\ d_{31} & d_{32} & d_{33} & 0 & 0 & 0 \end{bmatrix} \begin{bmatrix} T_1 \\ T_2 \\ T_3 \end{bmatrix} + \begin{bmatrix} \varepsilon_{11} & 0 & 0 \\ 0 & \varepsilon_{22} & 0 \\ 0 & 0 & \varepsilon_{33} \end{bmatrix} \begin{bmatrix} E_1 \\ E_2 \\ E_3 \end{bmatrix} \qquad (12)$$

3.2.3. State-Space Equation

State-space model:

$$\frac{dx}{dt} = Ax + Bu \qquad (13)$$
$$y = Cx + Du$$

From the above equation, the 'Parameter tunability' controls the runtime tunability level for A, B, C, D. 'Auto': Allow Simulink to choose the most appropriate tunability level. 'Optimised': Tunability is optimised for performance. 'Unconstrained': Tunability is unconstrained across the simulation targets.

Table 1: Parameters of PHLMVS.[8]	
Type	**Numerical and materials**
Pump size /mm	150 × 60 × 22
Pump material	PMMA
Check valve type	Umbrella valve
Check valve material	Silica gel
Diameter of metal substrate /mm	∅41
Thickness of metal substrate /mm	0.4
Metal substrate material	Brass
Sensing material	Silver
Diameter of PZT disc /mm	∅25
Thickness of PZT disc /mm	0.2
PZT disc material	Pb (ZrTi) O3
Height of chamber /mm	0.5
Driving waveform	Sine wave
Hydraulic cylinder size /mm	69.5 × 29 × 29

4. The Effect of Hydraulic fluid in the Piezoelectric Hydraulic chamber and Diaphragm stack by the External force

The mathematical equations will be utilized to calculate deformation, driving voltage (sinusoidal), flow rate, velocity, and sensing voltage. In the motor, the middle position is located between the inlet and outlet. This positioning is necessary to determine the sensing voltage more accurately in a steady-state stage for the piezoelectric hydraulic motor. Consequently, the velocity of the piezoelectric hydraulic motor can be derived from the sensing voltage (sinusoidal) of the piezoelectric diaphragm at this middle position. Since the driving frequency is significantly lower than the natural frequency of the piezoelectric diaphragm, the deformation at the center of the circular piezoelectric diaphragm is [8],

$$\delta = \frac{3d_{31}A_dU}{4\pi t^2} \qquad (14)$$

Where d_{31} is the piezoelectric constant, A_d is the area of the piezoelectric diaphragm driving unit, t is the thickness of the piezoelectric diaphragm, and U is the driving (sinusoidal) voltage. When the sensing unit and the driving unit are on the same piezoelectric PZT diaphragm, the sensing unit senses the deflection of the driving unit. Therefore, the sensing voltage of the sensing unit generated by displacement δ is

$$Us = h_{31}\delta = \frac{3h_{31}d_{31}A_dU}{4\pi t^2} \qquad (15)$$

The piezoelectric stiffness coefficient is represented by h_{31}. To simplify the analysis of the piezoelectric diaphragm, further improvements have been reduced to a thin plate problem. For ease of analysis, the ring force exerted on the piezoelectric diaphragm due to the driving voltage is considered as the output resultant force of the diaphragm [19]. The deformation of the piezoelectric diaphragm arises primarily from the output resultant forces of the diaphragm and the pressure exerted by the fluid on it. When the phases of these two forces (the voltage applied to the mass of the diaphragm and the mass of the hydraulic fluid) are identical, the deformation of the diaphragm is maximised. At this point, when the driving frequency ω equals the natural frequency ωn, the sensing voltage reaches its maximum value as a sinusoidal signal. Therefore, the optimal frequency of the system can be determined by identifying the frequency at which the maximum sinusoidal sensing voltage occurs. Based on Eq. (15), the maximum sensing voltage of the sensing unit can be expressed as follows:

$$U_{s,max} = h_{31}(\delta + \lambda\, y_{max}) \qquad (16)$$

The fluid impact coefficient can be described using Equations (15) and (16). When the parameters of the piezoelectric diaphragm remain constant, the sensing voltage (which is sinusoidal) has a linear relationship with the driving voltage (also sinusoidal) [19]. Additionally, the relationship between the sensing voltage and the output flow rate of the serially connected seven-chamber piezoelectric pump can be expressed as follows:

$$Q_g = \frac{\sqrt{5}\eta \Delta V \omega}{\pi} = \frac{\sqrt{5}\eta d^2 \omega U_s}{8h_{31}} \qquad (17)$$

The efficiency parameter of the check valve, denoted as 'Qg', represents the output flow rate of a seven-chamber piezoelectric pump connected in series. The symbol 'd' refers to the diameter of the piezoelectric diaphragm. The velocity of the fluid is influenced by both the flow rate of the piezoelectric motor and the effective area of the hydraulic cylinder piston [8]. Consequently, when there is an external load, the velocity of the liquid flow can be expressed as follows:

$$v = \left(1 - \frac{F}{F_{\max}}\right)\frac{Q_g}{A_c} \qquad (18)$$

Where Ac is the cross-sectional area of a hydraulic cylinder, F is the external load, and Fmax is the block force of the hydraulic cylinder. The velocity of the piezoelectric hydraulic motor decreases linearly with increasing external load. According to Eqs. (15), (17) and (18), the velocity of the piezoelectric hydraulic motor below external load can be derived as

$$v = \left(1 - \frac{F}{F_{\max}}\right)\frac{\sqrt{5}\eta d^2 \omega U_s}{8A_c h_{31}} \qquad (19)$$

According to Equation (19), once the driving parameters and the structure of the PZT material are established, the sensing voltage (which is sinusoidal) is proportional to the velocity under external loads. As the external load increases, the velocity of the piezoelectric hydraulic motor decreases. The equations mentioned are utilized to determine the parameters and constants, along with the Multiple Linear Regression (MLR) method, to calculate the sensing voltage.

Table 2: Hydraulic Chamber and Diaphragm Stack Parameters

(1)	(2)	(3)	(4)	(5)	(6)	(7) **(Y)**	(8)	(9)	(10) **(X1)**	(11) **(X2)**
Dia. Of Diaphragm (d) (mm)	**Thick. Of Diaphragm (t) (mm)**	**Area of Diaphragm (Ad) $(mm)^2$**	**Driving Frq (ω) (rad/sec)**	**Disp. of Diaphragm (sinusoidal) (U) (mm)**	**Driving Voltage (Us) (V)**	**Output Flowrate (Qg) (mm L/sec)**	**External Load (F) (kg/mm^2)**	**Blocking Force (F_{max}) (kg/mm^2)**	**Diaphragm Deformation (δ) (mm)**	**Vel. Of Hyd. Fluid (v) (mm/sec)**
26.17	0.65	534.92	0.01378	0.6285	0.01129	0.0534	0.8	15.57	5.323	1.3353E-2
27.0	2.10	572.62	0.004562	0.2081	0.01736	0.1715	1.5	27.1	1.389	4.271 E-2
25.0	2.50	490.94	0.003384	0.1545	0.00592	0.0105	2.5	37.8	1.677	2.585 E-2
25.4	5.10	506.77	0.002298	0.1048	0.12822	0.554	3.0	34.6	10.459	1.337 E-1
25.0	6.52	490.94	0.0016644	0.0759	0.0977	0.175	4.5	6.23	13.490	1.281 E-2
23.8	4.16	444.88	0.0015157	0.0691	0.03189	0.0568	10.0	14.10	3.652	4.354 E-3

The above data will be used to find the system performance using the Multiple Linear Regression **(MLR)** to find out the sensing voltage or sinusoidal values for the (A3/A4/A5).

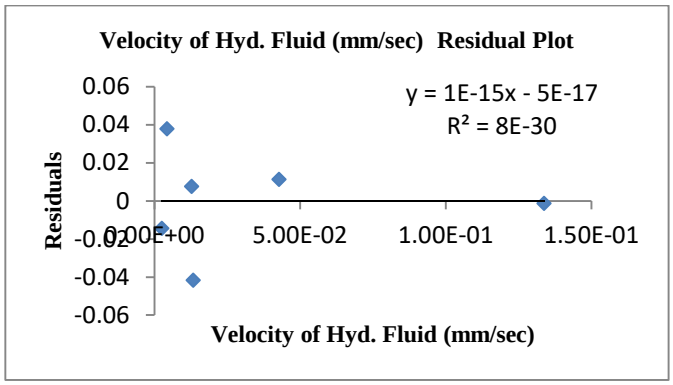

Fig 10: Velocity of Hyd. Fluid Vs Residual Plot.

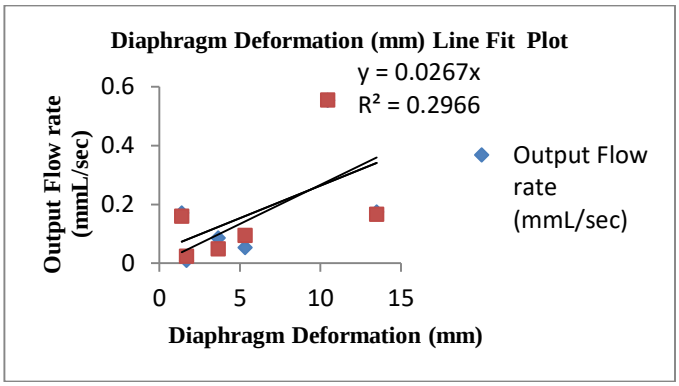

Fig 11: Diaphragm Deformation Line Fit Plot.

SUMMARY OUTPUT

Regression Statistics	
Multiple R	0.990739278
R Square	0.981564317
Adjusted R Square	0.969273861
Standard Error	0.03446366
Observations	6

ANOVA

	df	*SS*	*MS*	*F*	*Significance F*
Regression	2	0.189715828	0.094857914	79.86394851	0.002503161
Residual	3	0.003563232	0.001187744		
Total	5	0.19327906			

	Coefficients	*Standard Error*	*t Stat*	*P-value*	*Lower 95%*	*Upper 95%*	*Lower 95.0%*	*Upper 95.0%*
Intercept	0.000667485	0.023752657	0.028101472	0.979346086	-0.074924071	0.07625904	-0.074924071	0.07625904
Diaphragm Deformation (mm)	0.009093183	0.003364253	2.702883424	0.073606145	-0.001613371	0.019799738	-0.001613371	0.019799738
Velocity of Hyd. Fluid (mm/sec)	3.436229999	0.32893366	10.44657454	0.001872427	2.389416288	4.48304371	2.389416288	4.48304371

RESIDUAL OUTPUT

Observation	*Predicted Output Flow rate (mmL/sec)*	*Residuals*	*Standard Residuals*
1	0.094954479	-0.041554479	-1.556613611
2	0.1600593	0.0114407	0.428563901
3	0.024799408	-0.014299408	-0.535649904
4	0.555197041	-0.001197041	-0.044840672
5	0.167352636	0.007647364	0.286467102
6	0.048837136	0.037962864	1.422073184

PROBABILITY OUTPUT

Percentile	*Output Flow rate (mmL/sec)*
8.333333333	0.0105
25	0.0534
41.66666667	0.0868
58.33333333	0.1715
75	0.175
91.66666667	0.554

Fig 12: Multiple Linear Regression for the sensing voltage or sinusoidal signal using ANOVA Table.

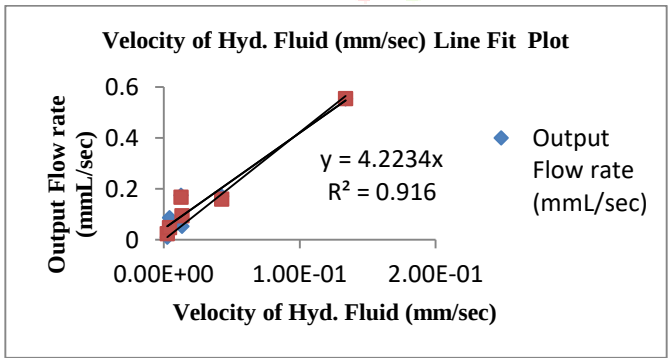

Fig 13: Velocity of Hyd. Fluid Line Fit Plot.

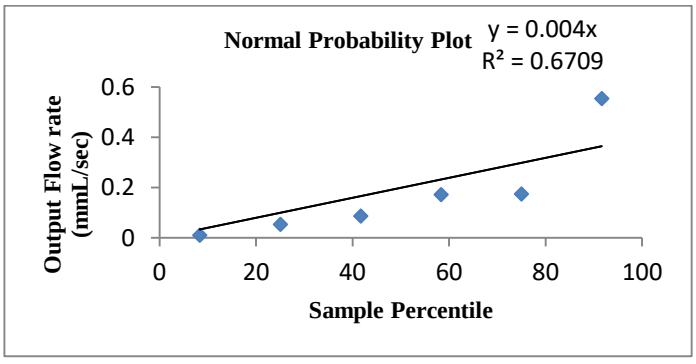

Fig 14: Normal Probability Plot

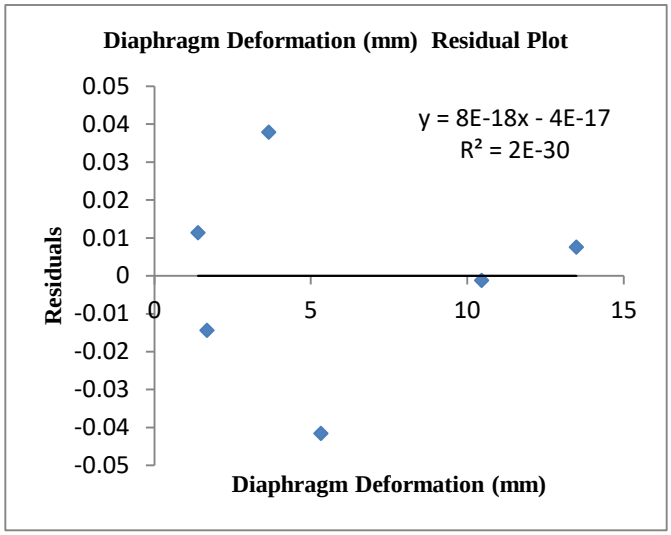

Fig 15: Diaphragm Deformation vs. Residual Plot

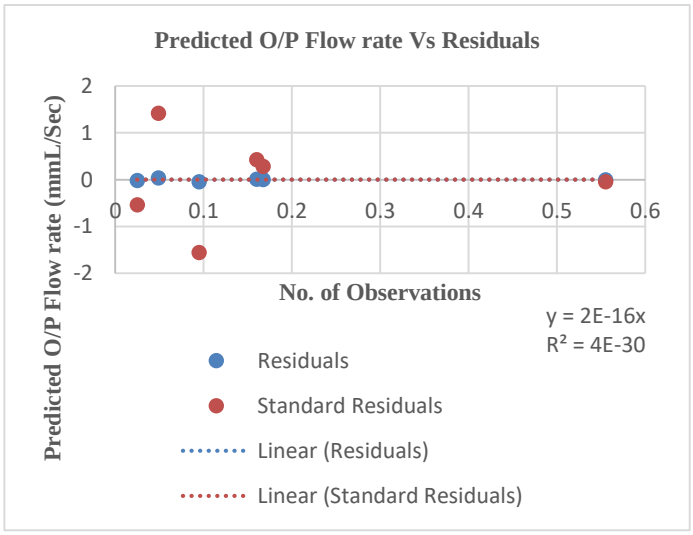

Fig 16: Predicted O/P Flow rate Vs Residuals.

Table 3: Summary of Decisions

S. No	Result Metric	Indicates	Results	Decision Action
1	High R-squared	Good fit	**High R^2adj (>0.9):** The model is reliable for prediction and control. **Low R^2adj (<0.7):** The relationship might be non-linear (e.g., in high-pressure scenarios where diaphragm behavior is non-linear), requiring non-linear regression.	Use the model for control & prediction
2	Sig. F<0.05	Valid model	If **the P-value is <0.05,** the Model is statistically significant the model is statistically significant.	Proceed with analysis
3	P-Value<0.05	Important variable	1)**P-value<0.05:** The factor (e.g., Deformation) significantly affects the output (e.g., Flow rate). 2)**P-value>0.05:** The factor is not significant. Decision: Remove this variable to simplify the model.	Retain/Control this factor
4	High β Value	High sensitivity	Allows for direct comparison of predictors measured on different scales.	Focus design/effort on this variable
5	High VIF (Variance Inflation Factor)	Redundant predictors	1)If **VIF is high (often >5 or 10**), it means independent variables (e.g., two different pressure gauges) are too highly correlated 2)**Decision:** Remove one to improve the stability and accuracy of the regression model.	Eliminate one predictor

The output of the Excel ANOVA model equation matches the MATLAB Model equation.

Output of the Excel ANOVA Model Equation	Output of the MATLAB Model Equation
Output Flowrate =0.000667+0.009093xDiaphragm Deformation+3.43623xVelocity of Hyd. Fluid	Y = 0.0007 + 0.0091*X1 + 3.4362*X2

5. Mathematic Modelling in MATLAB Simulink

5.1. System of Double-acting cylinder

The piezoelectric hydraulic diaphragm stack and the hydraulic chamber have been utilized to send signals to a 4/3 Direction control valve. This action activates the spool of the control valve, allowing it to position precisely, manage blocking force, and effectively control leakages of hydraulic fluid. Check valves are employed to guide the fluid in a specific direction, enabling the operation of the piezoelectric hydraulic diaphragm stack motor. The hydraulic system's power pack has been designed to support a double-acting cylinder with specified distance and force requirements. The Simulink model for the double-acting cylinder incorporates all necessary elements to achieve the desired outcomes. The forces and distances of both the piston and rod have been calculated. Additionally, the required dimensions for the cylinder, check valves, power pack, pipes, pressure relief valve, and direction control valve have been determined to analyze the necessary distances and forces for the systems involved.

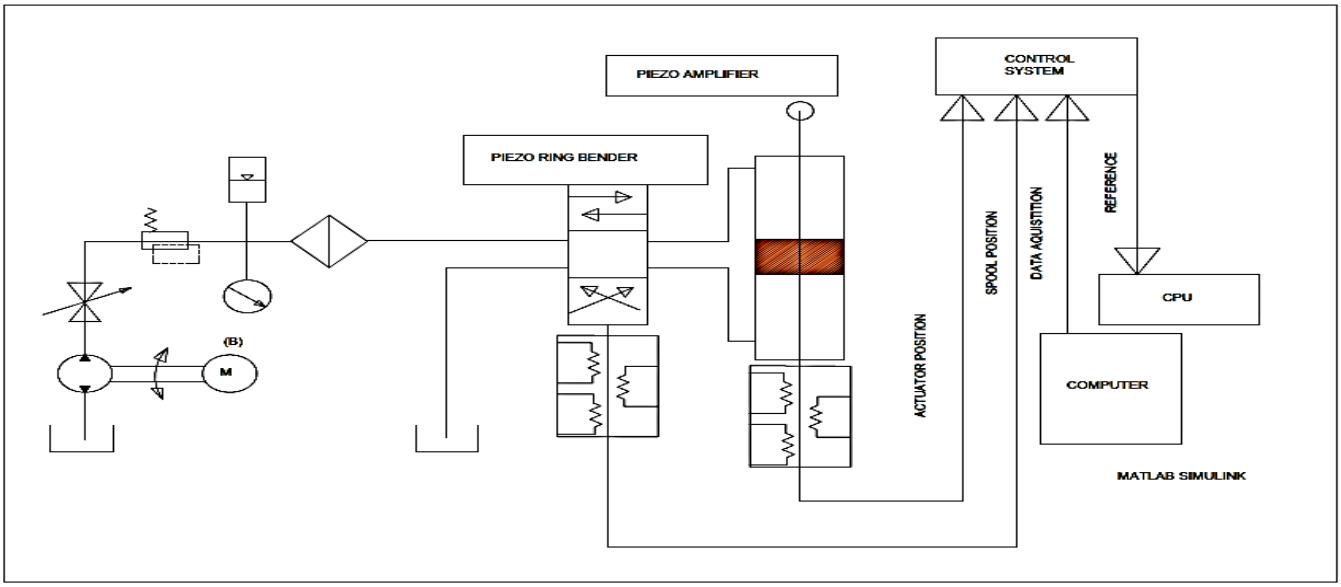

Fig 17. Semantic Diagram of Double-acting Cylinder with Piezoelectric Hydraulic motor [2], [10]

The MATLAB Simulink blocks were developed based on the semantical and free-body diagrams to achieve the desired output. This was accomplished by incorporating external non-linear noise, including white noise, along with relay, delay, and PID blocks to mitigate the noise and delay effects. The hysteresis behavior of the piezoelectric hydraulic diaphragm stack is managed using the Bouc-Wen hysteresis model. The Newton-Raphson method is employed in an iterative loop to obtain accurate results. By varying the stiffness of the springs and dampers, the hysteresis behavior is analyzed, utilizing experimental data and information from various research journals.

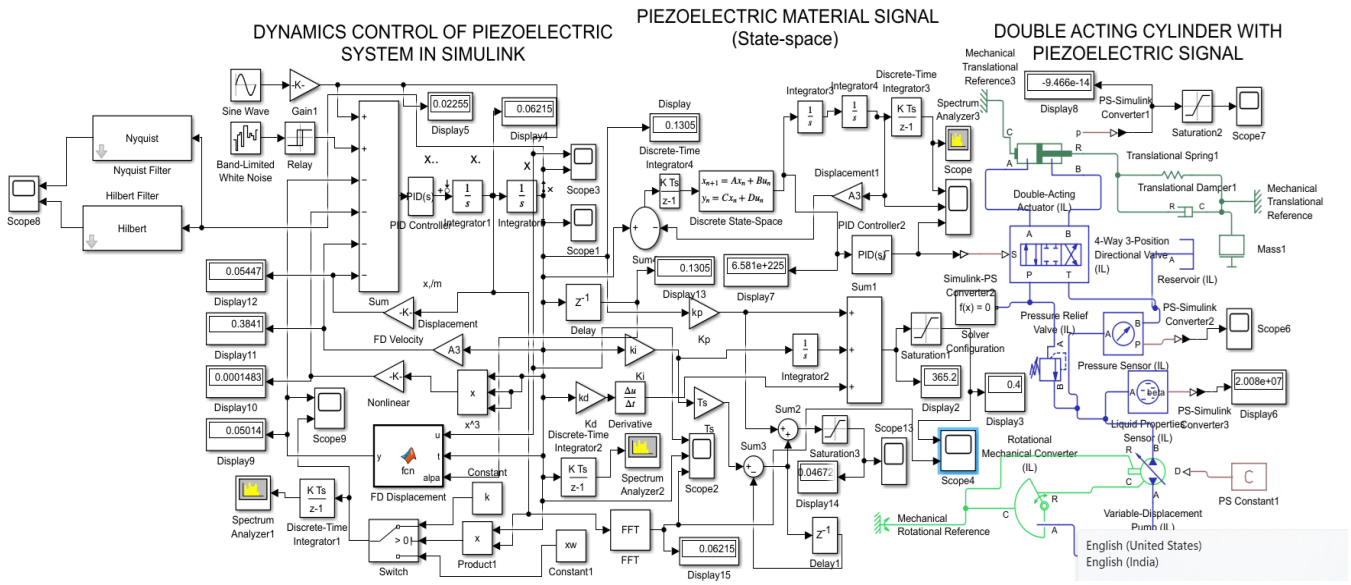

Fig 18: MATLAB Simulink for the 1. Dynamics control of the piezo-electric system 2. Piezoelectric material Signal (State-space) 3. Double-acting Cylinder with Piezoelectric signal

5.1.1. System Dynamics with the Piezoelectric Hydraulic Diaphragm Stack Material

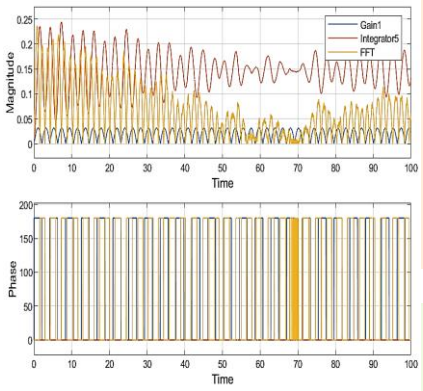

Fig 19: Gain Integrator and FFT - Plot

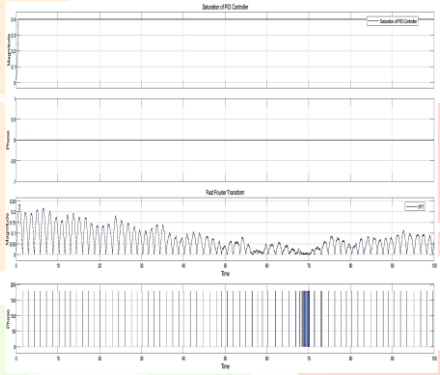

Fig 20: PID & FFT - Phase Magnitude

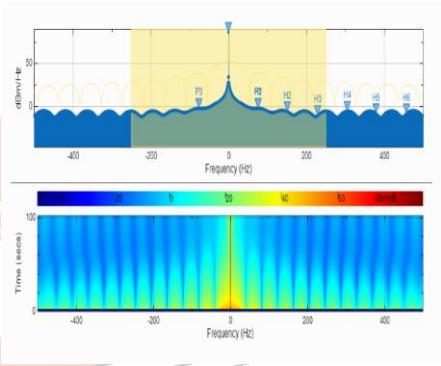

Fig 21: Spectrum Harmonic Distortion

By tuning the stiffness and damping values, the system can be placed in a stable state. The amplitude attenuation can be controlled using various techniques, such as P, PI, and PID methods. This process involves both forward and inverse feedback from sensors.

5.1.2. Verification of the system Mathematical model in MATLAB and analysis of its Stability

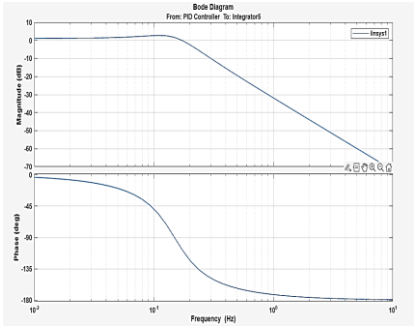

Fig 22: Bode Diagram

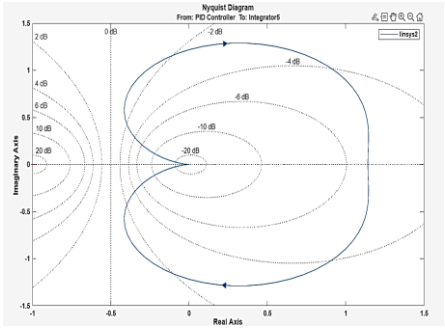

Fig 23: Nyquist Diagram

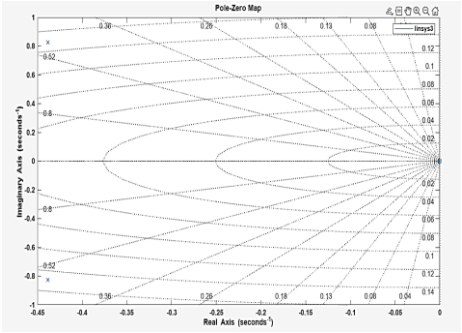

Fig 24: Pole-Zero Map

The stability of the system can be effectively assessed through the analysis of various graphical representations, such as the Bode plot, Nyquist diagram, and Pole-Zero map. In control theory, if the poles and zeros of the system are located in the left half of the s-plane, it indicates that the system is stable. This means that the system will respond to inputs without exhibiting unbounded growth or oscillations over time, leading to reliable and predictable performance. Analyzing these plots enables engineers to design and implement control strategies that ensure system stability under varying conditions.

5.1.3. Validated the stability and Mapping of the system with Experimental data

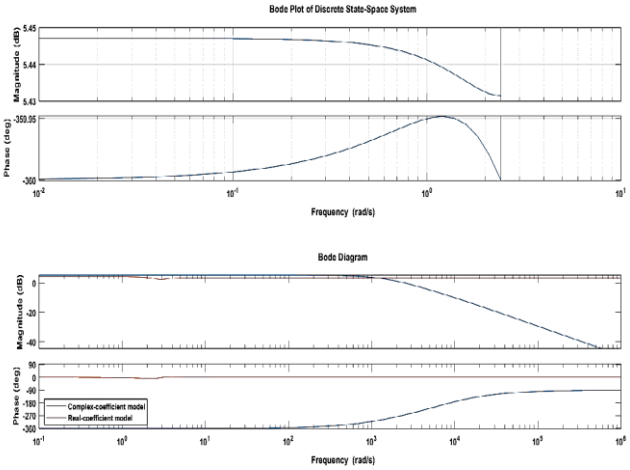

Fig 25: Bode Plot for the Experimental-1 Data

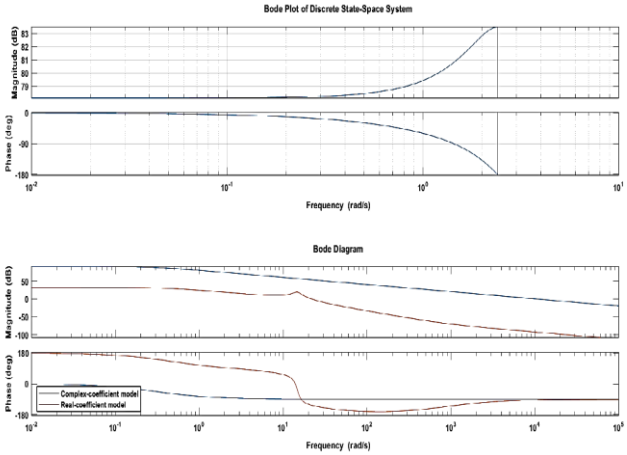

Fig 26: Bode Plot for the Experimental-2 Data

5.2. Piezoelectric Hydraulic Diaphragm Stack Hysteresis Analysis

5.2.1. Bouc-Wen Hysteresis Mathematical equations [17]

The dynamic behaviour of a piezo stack is commonly modelled as a second-order system combined with a hysteresis non-linear component.

$$m\ddot{x} + b\dot{x} + kx = k(du - h) \qquad (20)$$

Where m, b, and k are equivalent mass, damper, and stiffness of the stack/diaphragm system. du is linear piezoelectric displacement. 'h' is the Hysteresis operator defined by a differential equation.

$$\dot{h} = \alpha * d\dot{u} - \beta\left|\dot{u}\right|h[h]^{n-1} - \gamma\dot{u}[h]^{n} \qquad (21)$$

s

Where α, β, Υ are parameters determining the shape of the Hysteresis loop (Shape factor). u(dot) is the time derivative of the input sinusoidal signal.

5.2.2. Hysteresis Analysis using the Bouc-Wen Model

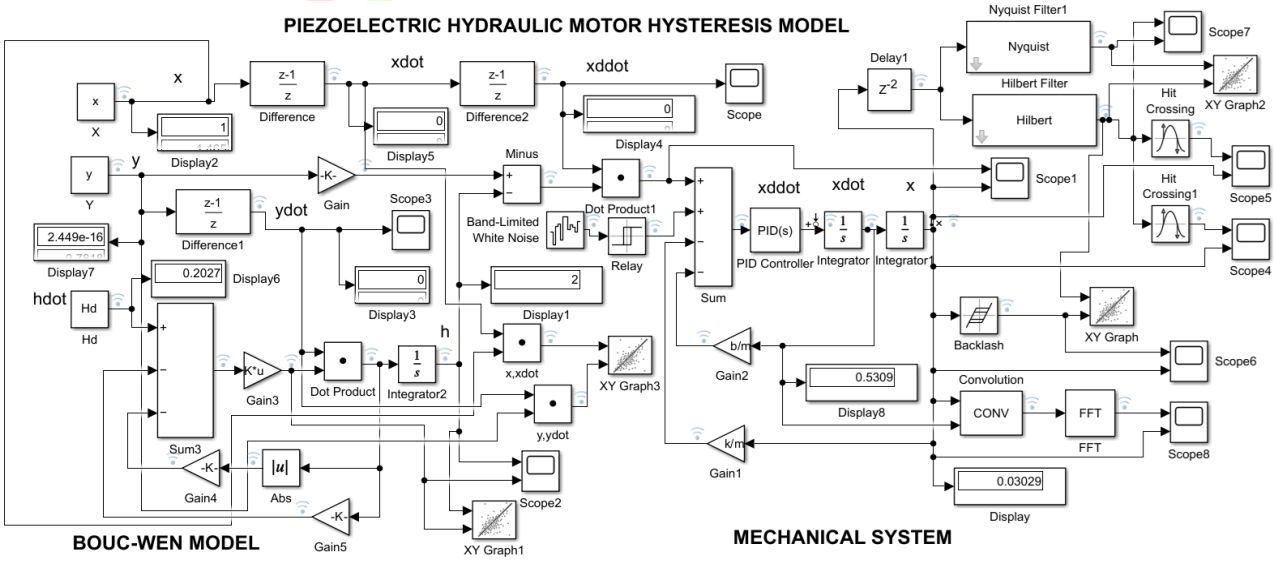

Fig 27: Hysteresis analysis for the Piezoelectric hydraulic diaphragm using the Bouc-Wen Model

5.2.3. Plots of the Bouc-Wen Model used in the Piezoelectric Hydraulic Diaphragm for Hysteresis Analysis

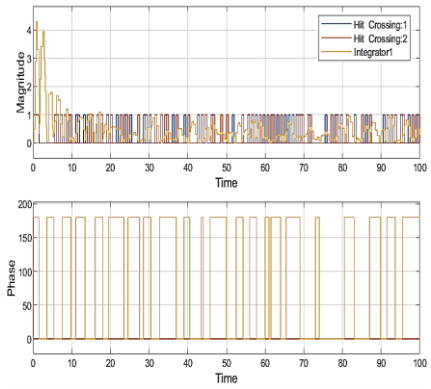

Fig 28: Hit Crossing Amplitude Vs Time

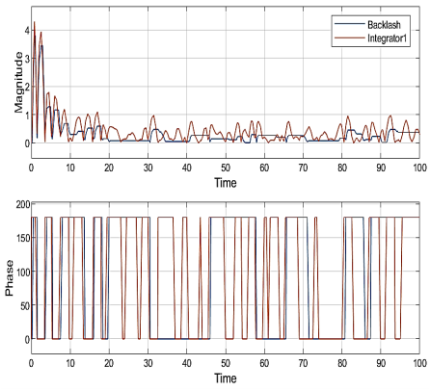

Fig 29: Time Vs Phase and Magnitude

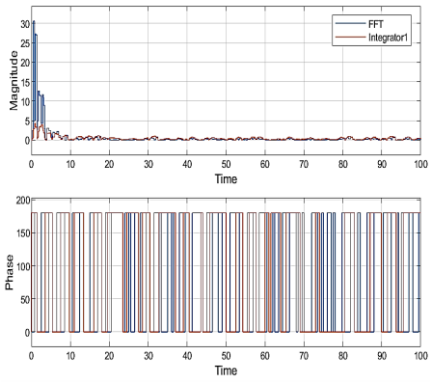

Fig 30: FFT Plot – Phase and Magnitude

5.2.4. Verification of Piezoelectric material Hysteresis Characteristic of the System and its stability in MATLAB

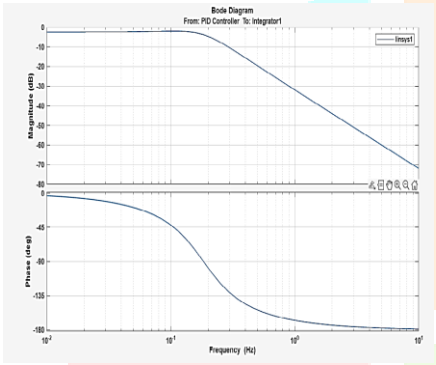

Fig 31: Bode Diagram

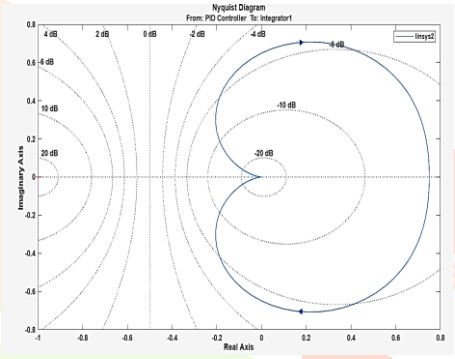

Fig 32: Nyquist Diagram

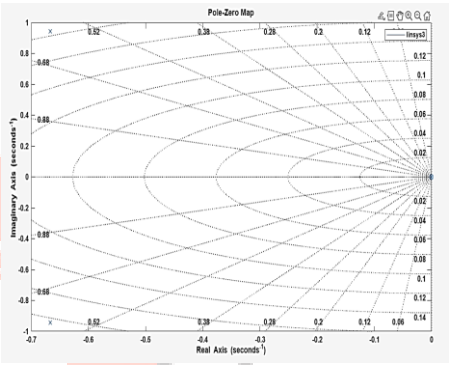

Fig 33: Pole-Zero Map

The stability of the system can indeed be evaluated through several key graphical methods, including the Bode plot, Nyquist diagram, and pole-zero map. When analyzing these plots, if all poles are located in the left half of the complex plane (left S-plane) while zeros are also accordingly placed, this indicates that the system is stable. Specifically:

Bode Plot: This provides insight into the frequency response of the system, where a stable system typically demonstrates a phase margin greater than zero, which helps mitigate the risk of oscillations or instability.

Nyquist Diagram: By plotting the frequency response, it becomes possible to check for encirclements of the critical point (-1, 0) in the complex plane. A stable system will not encircle this point in a clockwise direction.

Pole-Zero Map: Here, the positions of the system's poles and zeros are plotted in the complex plane. If all poles are in the left S-plane, it confirms the system's stability.

In summary, the verification of pole and zero placement in the left S-plane is a fundamental criterion for ensuring that the system operates stably.

5.2.5. Validated Hysteresis Behaviors of the Piezoelectric Hydraulic Diaphragm Stack

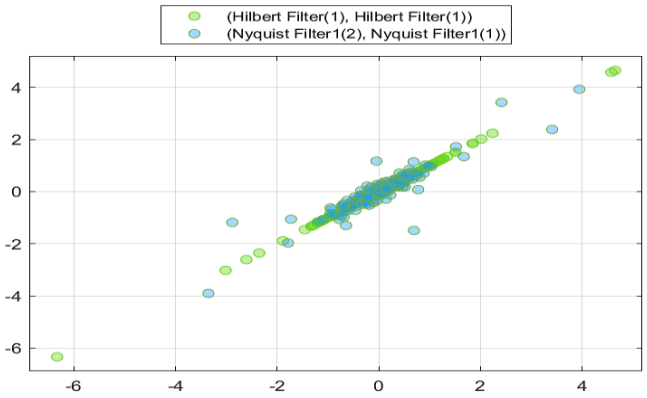

Fig 34: Hysteresis Characteristic of Piezoelectric Material

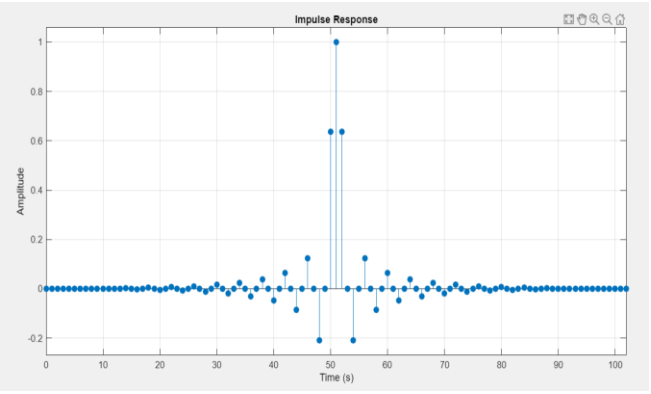

Fig 35: Impulse Response of the Piezoelectric Material

5.2.6. Comparison of Flowrate, Displacement, % Error and Frequency

Table 4. Comparison of the flow rate measured using a flowmeter with the theoretical value [2], [5]

Frequency (Hz)	Experimental Pumping Displacement (mm)	Theoretical Flowrate (mL/min)	Flow rate using Measuring Cylinder (mL/min)	Flowrate using Flowmeter (mL/min)	%error between the flow meter and theoretical value
1.0	369.0	25.550	25.2	25.36	0.75
2.0	366.0	49.810	50.4	49.10	1.45
3.0	360.0	73.490	72.4	70.95	3.58
4.0	350.0	95.264	93.6	92.80	2.66
5.0	340.5	115.850	114.0	113.10	2.43

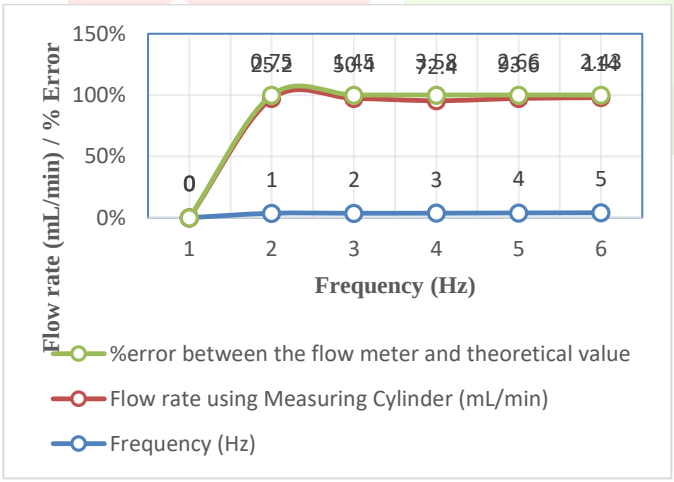

Fig 36: Frequency Vs Flowrate and % Error

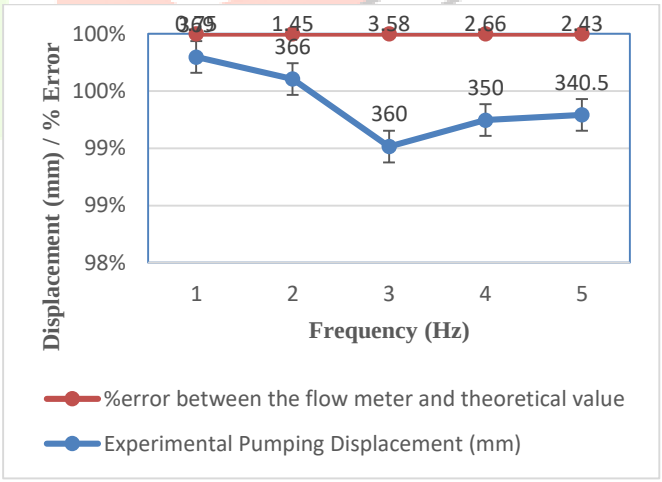

Fig 37: Frequency Vs Displacement and % Error

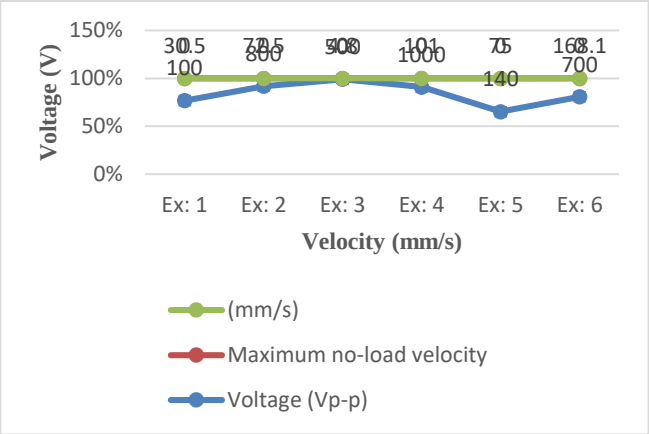

Fig 38: Velocity (mm/s) Vs Voltage (V)

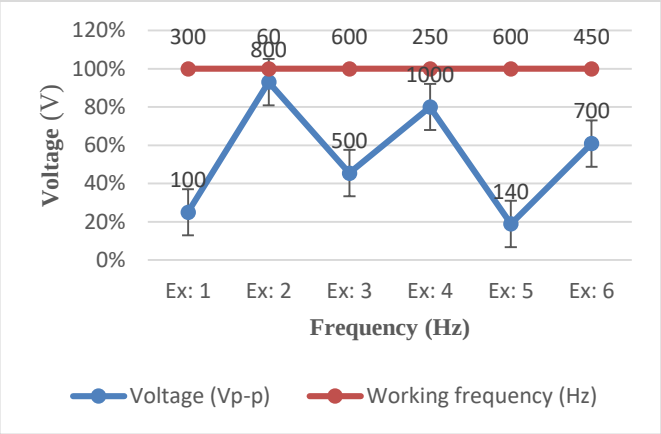

Fig 39: Frequency (Hz) Vs Voltage (V)

6. Piezoelectric Hydraulic Diaphragm analysis using ANSYS

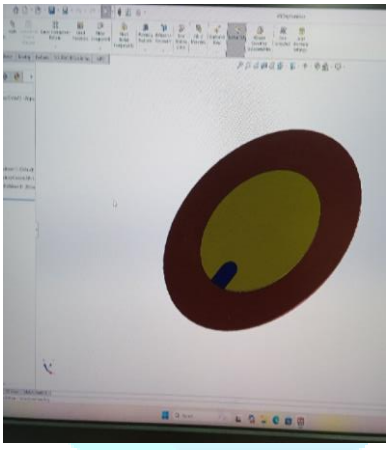

Fig 40: 3D Model of Diaphragm in Solid Works.

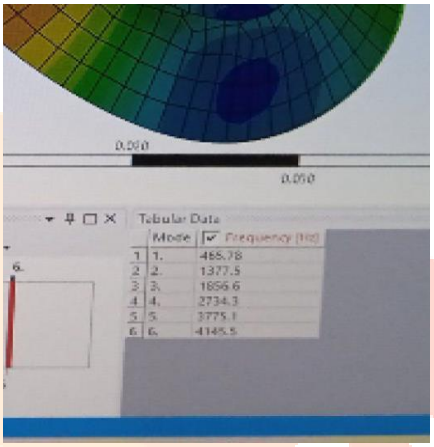

Fig 41: 3D Model Analysis in ANSYS.

Fig 42: Deformation of PZT Diaphragm

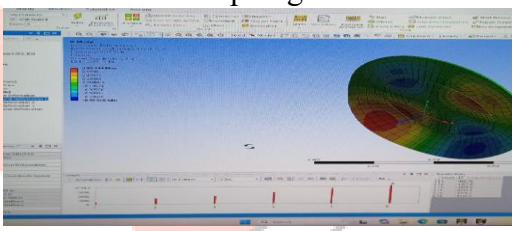

Fig 43: 6 Mode Shape of the Diaphragm in ANSYS

6.1.1. Frequency Mode analysis of Piezoelectric Hydraulic Diaphragm in ANSYS

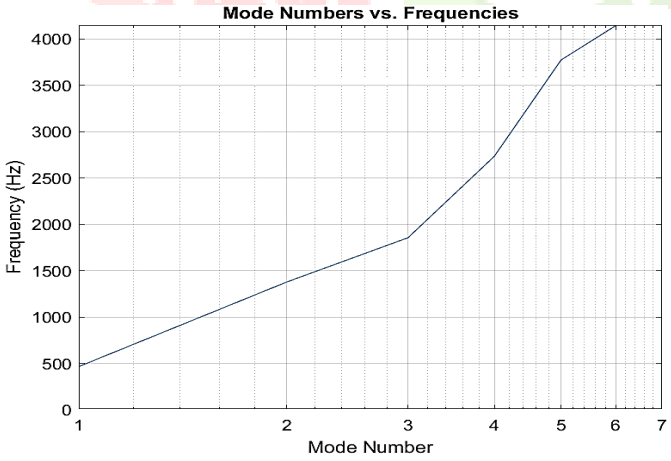

Fig 44: Semi-log(x) Plot analysis of Mode Numbers and Frequency (Hz) in the ANSYS software

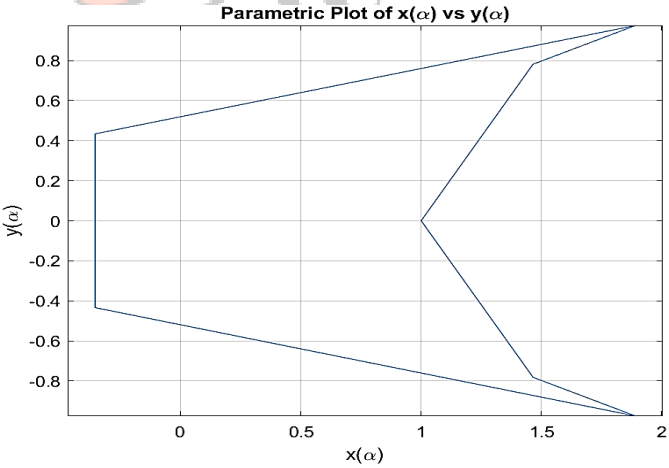

Fig 45: Parametric Plot for Alpha Values in (X-axis and Y-axis) in MATLAB.

6.1.2. Piezoelectric Hydraulic diaphragm stack Characteristics against Blocking force: a Comparison

Table 5. Comparison of the proposed hybrid actuator and other hybrid actuators [2], [19]

Parameters	Sirohi and Chopra[13]	Mauck and Lynch[14]	Diao et al.[17]	Xuan et al.[32]	John et al.[33]	The proposed Actuator
Voltage (Vp-p)	100	800	500	1000	140	700
Working frequency (Hz)	300	60	600	250	600	450
Maximum no-load velocity (mm/s)	30.5	72.5	4.8	101	75	168.1
Maximum blocking force (N)	155.7	271	378	346	62.3	141

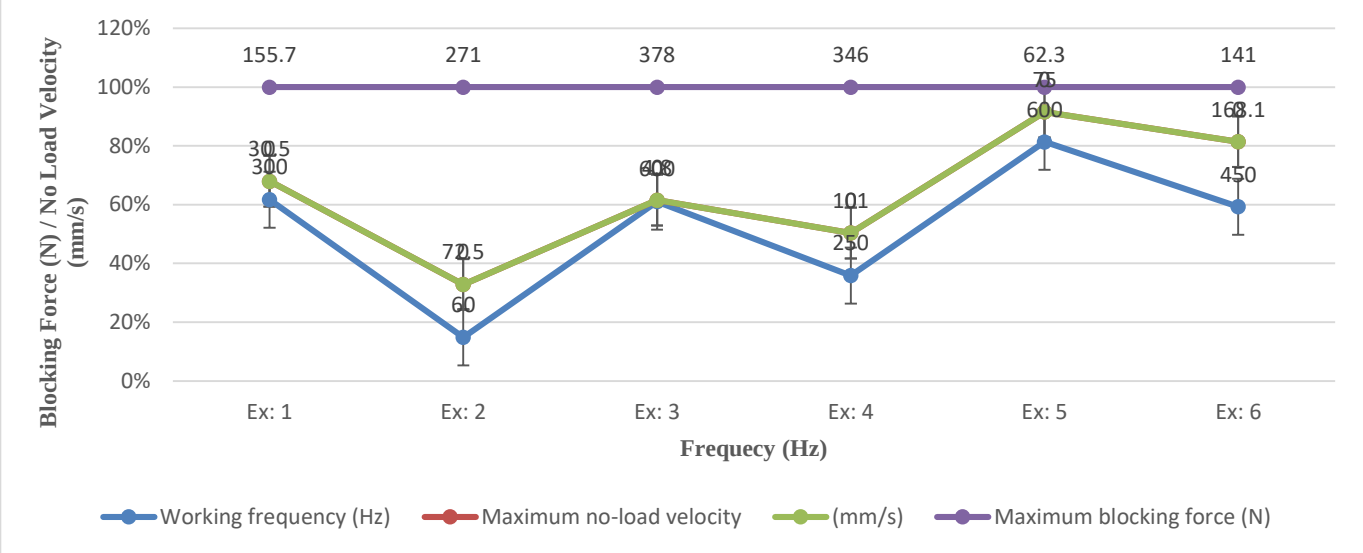

Fig 46: Plot for the Working Frequency (Hz) Vs Blocking Force (N) and No-Load Velocity (mm/s)

7. Comparison of the results and discussion

7.1. Flow rate of the piezoelectric Hydraulic Diaphragm Stack motor

Under a fixed sinusoidal voltage magnitude, the driving frequency ranges from 0 to 600 Hz. The flow rate and sensing voltages of piezoelectric diaphragms A1, A3, A5, and A7 are illustrated in Fig. 36. When the driving frequency ranges from 0 to 480 Hz, the flow rate increases as the frequency increases. At 480 Hz, a peak flow rate is observed, with a maximum measurement of 110.11 ml/min. However, beyond 480 Hz, the flow rate begins to decrease as the driving frequency continues to increase. The sensing voltages for diaphragms A3, A5, and A7 change with the driving frequency and reach their maximum values. In contrast, the sensing voltage for diaphragm A1 shows an upward trend with increasing frequency, which is not consistent with the flow rate trend. When the driving frequency is held constant at 480 Hz, and the driving voltage varies between 100 and 300 V, the flow rate and sensing voltages for diaphragms A1, A3, and A5 are depicted in Fig. 38. Both the flow rate and the sensing voltages (sinusoidal) for A1, A3, and A5 increase as the driving voltage is increased. Notably, when the driving voltage is set to 100 V, the frequency is 300 Hz.

7.2. Frequency Characteristic

Figure 46 illustrates the relationship between velocity and frequency for the Piezoelectric hydraulic motor under different external loads at a fixed voltage of 2.00 V. It is evident that as the driving frequency increases, the velocity of the motor initially rises before beginning to decline. For external loads of 0 N, 50 N, and 100 N, the maximum velocities occur at optimal frequencies of 200 Hz, 300 Hz, and 600 Hz, respectively. The observed maximum velocities are 4.8 mm/s, 30.5 mm/s, and 168.1 mm/s for these loads. Notably, as the external load increases, the optimal frequency required for the motor also increases, while the maximum velocity tends to decrease.

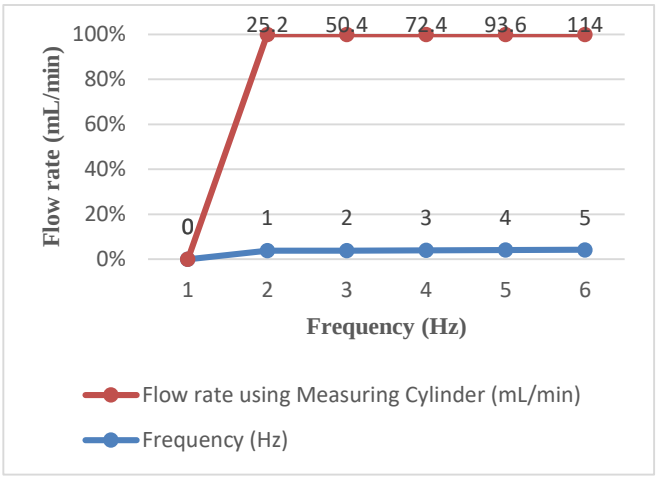

Fig 47: Frequency (Hz) Vs Flow rate (mL/min)

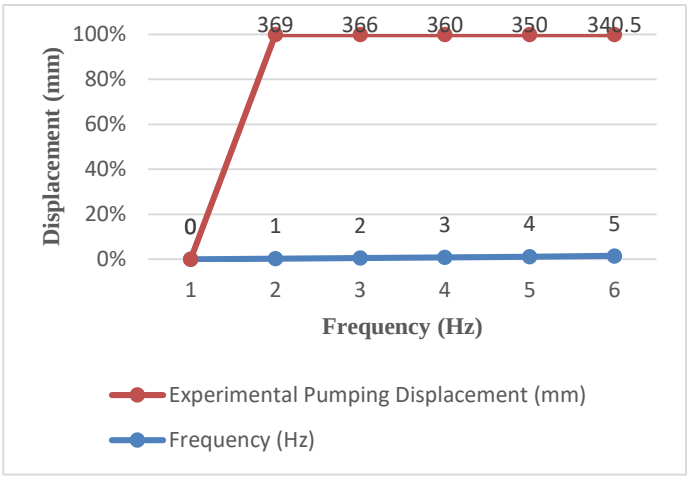

Fig 48: Frequency (Hz) vs Displacement (mm)

The validation of the simulation results for the piezoelectric hydraulic diaphragm motor involved several specific experimental methods and numerical data, including:

Physical Experimentation: This included the construction of a prototype of the piezoelectric hydraulic diaphragm motor. Various performance metrics were collected during experimentation under different load conditions to ensure the validity of the simulated data.

Comparative Analysis: The experimental results were compared with the numerical data obtained from simulations. Discrepancies between the two were analyzed to adjust the simulation parameters for better accuracy.

Flow Rate Measurement: Measurements of flow rates from the piezoelectric diaphragms were taken during experiments to correlate with the simulation outputs, particularly focusing on the middle three diaphragms (A3, A4, and A5).

Voltage and Frequency Testing: Different excitation voltages (ranging from 100V to 1000V) and frequencies (from 60 Hz to 600 Hz) were applied during experiments to assess the motor's response and functional efficiency, ensuring that the simulation results were consistent across varying conditions.

Pressure Testing: The stability and performance under differing external loads were tested to capture how changes in load impacted the motor's operation and performance, further validating the model's reliability.

These methods worked together to establish a strong correlation between simulated results and real-world performance, confirming the efficacy of the motor design and its operational parameters.

7.3. Displacement Characteristic

The data presented in Fig. 46 shows the velocity and A3/A4/A5 sensing voltage of the piezoelectric hydraulic diaphragm when driven at a frequency of 500 Hz with an external load of 50 N. The driving voltage varies between 100 V and 300 V. As the driving voltage increases, both the velocity and the A3/A4/A5 sensing voltage also increase. There is a strong linear relationship between the A3/A4/A5 sensing voltage and driving voltage. At a driving voltage of 100 V, the velocity is measured at 30.5 mm/s with an A3/A4/A5 sensing voltage of 800 V. When the driving voltage rises to 800 V, the velocity increases to 72.5 mm/s, while the A3/A4/A5 sensing voltage changes to 500 V. To further investigate the linear relationship between the velocity of the piezoelectric hydraulic motor and the A3/A4/A5 sensing voltage under different external loads, while maintaining a fixed frequency of 500 Hz, the Multiple Linear Regression (MLR) method is employed. This analysis, depicted in Figs. 10–16, shows that with external loads of 0, 50, and 100 N, there is a clear linear relationship between the A3/A5 sensing voltage and velocity.

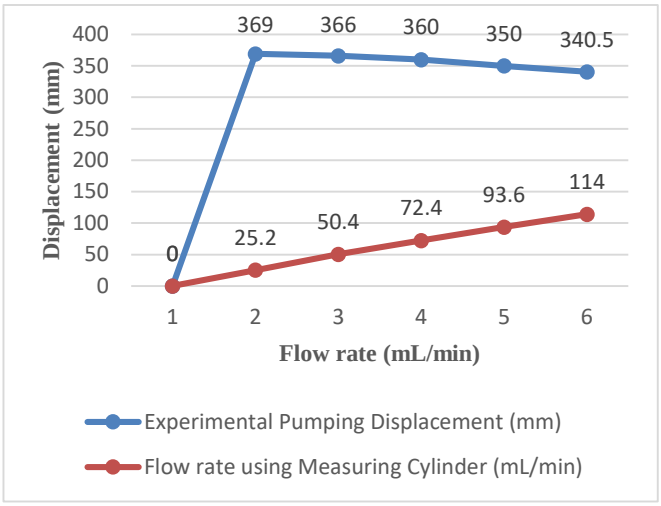

Fig 49: Displacement (mm) Vs Flow rate (mL/min)

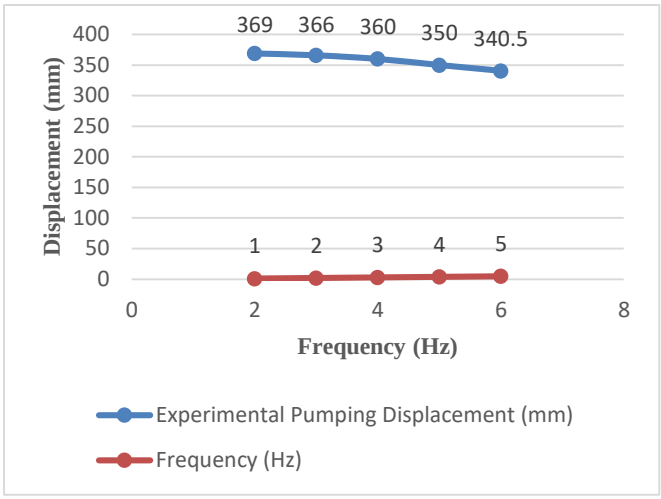

Fig 50: Displacement (mm) Vs Frequency (Hz)

8. Conclusion

A piezoelectric hydraulic diaphragm motor featuring a velocity display has been developed, with experimental data providing insights into the flow rate of the serially connected seven-chamber piezoelectric hydraulic diaphragm stack pump. The analysis reveals that the sensing voltage signals from chambers A3, A5, and A7 generated by a sinusoidal input exhibited a strong correlation with the flow rate. Further investigation was conducted to explore the relationship between the A3, A5, and A7 sensing voltage (sinusoidal) and the motor's velocity, varying different driving frequencies and voltages. The data from Tables 2, 3, and 4 indicate that the piezoelectric hydraulic diaphragm stack yielded optimal performance when driven by a fixed sinusoidal voltage ranging from 100V to 1000V, across a frequency span of 60 Hz to 600 Hz. Specifically, the optimal frequencies under external loads of 0.8 Kg/mm², 3.0 Kg/mm², and 10 Kg/mm² were determined to be 0.01378 rad/s, 0.004562 rad/s, and 0.003384 rad/s, respectively. The corresponding flow rates reached by the optimal frequencies of chambers A3, A5, and A7 were 0.554 mm³/s, 0.175 mm³/s, and 0.1715 mm³/s. This investigation thoroughly analyzed the flow rate, frequency characteristics, and displacement behaviours of the piezoelectric hydraulic diaphragm stack, enhancing the understanding of its operational capabilities.

Declaration of Competing Interest

The authors declare that they have no known competing financial interests or personal relationships that could have appeared to influence the work reported in this paper.

References

[1] C. Cadou and B. Zhang, “Performance Modeling of a Piezo-Hydraulic Actuator,” *J. Intell. Mater. Syst. Struct.*, vol. 14, no. 3, pp. 149–160, Mar. 2003, doi: 10.1177/1045389X03014003003.

[2] V. K. Sri Murali and Dr. K. Gokul Kumar, “REVIEW OF PIEZO HYDRAULIC MOTORS AND THEIR APPLICATIONS,” *Int. J. Creat. Res. THOUGHTS*, vol. 14, no. 1, 2026, doi: 10.56975/ijcrt.v14i1.300747.

[3] X. L. Jin *et al.*, “Experimental Study on the Performance of a Bidirectional Hybrid Piezoelectric-Hydraulic Actuator,” *Int. J. Aeronaut. Space Sci.*, vol. 16, no. 4, pp. 520–528, Dec. 2015, doi: 10.5139/IJASS.2015.16.4.520.

[4] P. Mercorelli and N. Werner, “Integrating a piezoelectric actuator with mechanical and hydraulic devices to control camless engines,” *Mech. Syst. Signal Process.*, vol. 78, pp. 55–70, Oct. 2016, doi: 10.1016/j.ymssp.2015.12.038.

[5] S. Nayak and M. Rao, “Design and development of a flexurally amplified piezoelectric actuator based piezo-hydraulic pump,” *Mater. Today Proc.*, vol. 46, no. xxxx, pp. 9956–9965, 2021, doi: 10.1016/j.matpr.2021.03.314.

[6] L. D. Mauck and C. S. Lynch, “Piezoelectric Hydraulic Pump Development,” *J. Intell. Mater. Syst. Struct.*, vol. 11, no. 10, pp. 758–764, Oct. 2000, doi: 10.1106/HC2A-ABR9-21H8-2TJB.

[7] J. Kan *et al.*, “Development of piezohydraulic actuator driven by piezomembrane pump,” *J. Intell. Mater. Syst. Struct.*, vol. 22, no. 16, pp. 1829–1840, Nov. 2011, doi: 10.1177/1045389X11414074.

[8] C. Qian, S. Chen, J. Wang, J. Kan, Z. Zhang, and M. Yu, "A piezoelectric hydraulic linear motor with velocity self-monitoring," *Sens. Actuators Phys.*, vol. 306, p. 111962, May 2020, doi: 10.1016/j.sna.2020.111962.

[9] Z. Xuan *et al.*, "Performance of piezo-stacks for a piezoelectric hybrid actuator by experiments," *J. Intell. Mater. Syst. Struct.*, vol. 25, no. 18, pp. 2212–2220, Dec. 2014, doi: 10.1177/1045389X14533439.

[10] F. Stefanski, B. Minorowicz, J. Persson, A. Plummer, and C. Bowen, "Non-linear control of a hydraulic piezo-valve using a generalised Prandtl–Ishlinskii hysteresis model," *Mech. Syst. Signal Process.*, vol. 82, pp. 412–431, Jan. 2017, doi: 10.1016/j.ymssp.2016.05.032.

[11] Hwee Choo Liaw, B. Shirinzadeh, and J. Smith, "Robust Neural Network Motion Tracking Control of Piezoelectric Actuation Systems for Micro/Nanomanipulation," *IEEE Trans. Neural Netw.*, vol. 20, no. 2, pp. 356–367, Feb. 2009, doi: 10.1109/TNN.2008.2004406.

[12] J. M. McCarthy, S. Watkins, A. Deivasigamani, and S. J. John, "Fluttering energy harvesters in the wind: A review," *J. Sound Vib.*, vol. 361, pp. 355–377, Jan. 2016, doi: 10.1016/j.jsv.2015.09.043.

[13] Q. Zhang, W. Ruan, H. Wang, Y. Zhou, Z. Wang, and L. Liu, "A self-bended piezoresistive microcantilever flow sensor for low flow rate measurement," *Sens. Actuators Phys.*, vol. 158, no. 2, pp. 273–279, Mar. 2010, doi: 10.1016/j.sna.2010.02.002.

[14] K. Higuchi, "A piezoelectric linear motor driven by superposing standing waves with phase difference," in *36th Structures, Structural Dynamics and Materials Conference*, New Orleans,LA,U.S.A.: American Institute of Aeronautics and Astronautics, Apr. 1995. doi: 10.2514/6.1995-1110.

[15] O. Fuchs *et al.*, "A novel volumetric silicon micropump with integrated sensors," *Microelectron. Eng.*, vol. 97, pp. 375–378, Sep. 2012, doi: 10.1016/j.mee.2012.04.036.

[16] Z. Zhang, J. Kan, G. Cheng, H. Wang, and Y. Jiang, "A piezoelectric micropump with an integrated sensor based on space-division multiplexing," *Sens. Actuators Phys.*, vol. 203, pp. 29–36, Dec. 2013, doi: 10.1016/j.sna.2013.08.027.

[17] O. Français and I. Dufour, "Dynamic simulation of an electrostatic micropump with pull-in and hysteresis phenomena," *Sens. Actuators Phys.*, vol. 70, no. 1–2, pp. 56–60, Oct. 1998, doi: 10.1016/S0924-4247(98)00112-5.

[18] Z. Zhang, J. Kan, S. Wang, H. Wang, J. Wen, and Z. Ma, "Flow rate self-sensing of a pump with double piezoelectric actuators," *Mech. Syst. Signal Process.*, vol. 41, no. 1–2, pp. 639–648, Dec. 2013, doi: 10.1016/j.ymssp.2013.08.012.

[19] J. Kan, K. Tang, G. Liu, G. Zhu, and C. Shao, "Development of serial-connection piezoelectric pumps," *Sens. Actuators Phys.*, vol. 144, no. 2, pp. 321–327, Jun. 2008, doi: 10.1016/j.sna.2008.01.016.

[20] J. Kan, K. Tang, Y. Ren, G. Zhu, and P. Li, "Study on a piezohydraulic pump for linear actuators," *Sens. Actuators Phys.*, vol. 149, no. 2, pp. 331–339, Feb. 2009, doi: 10.1016/j.sna.2008.12.008.

[21] G. Nader, E. C. N. Silva, and J. C. Adamowski, "Effective Damping Value of Piezoelectric Transducer Determined by Experimental Techniques and Numerical Analysis".

[22] P. Albrecht-Zagar and R. Scheidl, "A Piezo-Electric Valve Actuator for Hydraulic Exoskeleton Drives," *Int. J. Fluid Power*, Sep. 2022, doi: 10.13052/ijfp1439-9776.23310.